Annals of Biomedical Engineering
https://doi.org/10.1007/s10439-026-04317-0

BMES BIOMEDICAL ENGINEERING SOCIETY

ORIGINAL ARTICLE

Fluid–Structure Interaction Analysis of Human Eye with Descemet Membrane Detachment

Ammar I. Alsabery[1] · **Muneer A. Ismael**[2,3] · **Zehba Raizah**[4] · **Mohammad Ghalambaz**[5] · **Ishak Hashim**[6,7]

Received: 26 July 2025 / Accepted: 22 July 2026

Abstract

Detachment of Descemet membrane (DM) is a defect that occurs in the cornea of the human eye. Most previous examinations have focused on relatively simple benchmarks, excluding the complex interaction between intraocular fluid flow and delicate ocular structures such as the Descemet membrane, particularly in detachment issues. This paper simulates the detached DM as a flexible membrane to explore the convection inside the anterior chamber (AC) of human eye and to evaluate the cornea transplantation processes. The analysis is conducted numerically by considering the mixed heat transmission and the fluid–structure interaction (FSI) within a geometry representing the AC. The study of FSI facilitates the simulation of different elasticity modulus E of the detached DM ($E = 10^8$ to 10^{11}), which enables the study of various corneas implemented in transplantation processes. Rayleigh number is varied from 10^3 to 10^6 to simulate thermal therapy of temperature difference from 0.25 to 250 K. The length of the iris accounts the length of the contacting part of the lens S having the isothermal hot temperature is also explored. Results reveal that the cornea type affects the stress imparted on the DDM and does not affect the thermal characteristics or the displacement within the anterior chamber. The shrinkage of the iris elevates the convective thermal characteristic by about 78%. Elevating the thermal therapy ΔT from 2.5 to 25 K promotes the heat transfer by 47.6%.

Keywords Anterior chamber flow · Descemet membrane detachment · FSI · Human eye · Cornea

Introduction

Thermal therapy and understanding the rapture risk in the medical field are important clinical management, contributing to treating eye diseases [1] and controlling blood flow through arteries [2]. The human eye components and the walls of arteries are flexible nature structured. To simulate the flow of fluid and the heat transfers in these applications, fluid–structure interaction (FSI), a phenomenon in which the deformation of solid structures under fluid flow is a robust procedure integrated with computational fluid dynamics (CFD). Fluid–structure interaction (FSI) and computational fluid dynamics (CFD) models have been involved in simulating fluid flow and structural behavior in different biological procedures, including the human eye [3, 4] and biological blood flow within artery [5–7]. Ferroni et al. [3] compared FSI and CFD analyses to investigate corrosion on the external surfaces of an intraocular injected device. They adopted the fluid–solid interaction feature of the FSI approach to simulate the relative motion between the inserted device and the vitreous, resulting from saccadic and eye rotations. They showed

Associate Editor Joel Stitzel oversaw review of this article.

✉ Ammar I. Alsabery
ammar_e_2011@yahoo.com

1 Refrigeration & Air-Conditioning Technical Engineering Department, College of Technical Engineering, The Islamic University, Najaf, Iraq

2 Mechanical Engineering Department, Engineering College, University of Basrah, Basra 61004, Iraq

3 College of Engineering, University of Warith Al-Anbiyaa, Karbalā’, Iraq

4 Department of Mathematics, College of Science, King Khalid University, Abha, Saudi Arabia

5 Department of Mathematical Sciences, Saveetha School of Engineering, SIMATS, Chennai, India

6 Department Mathematical Sciences, Faculty of Science & Technology, Universiti Kebangsaan Malaysia, UKM, 43600 Bangi, Selangor, Malaysia

7 Nonlinear Dynamics Research Center (NDRC), Ajman University, PO Box 346, ʿAjman, United Arab Emirates

that the wall shear stress induced by flow in the FSI analysis was lower than that in the CFD analysis, attributing this to the disregarded relative motion in the latter analysis. However, minor differences were reported between the two approaches (FSI and CFD) in predicting corrosion of the magnesium device. CFD and FSI approaches are also explored in a specific medial application: heart valve design. Luraghi et al. [5] demonstrated that fluid–structure interaction (FSI) simulations are more efficient than computational fluid dynamics (CFD) in enhancing various stages of prosthetic heart valve design and developing improved standards for the preclinical assessment of medical devices. This implies that computational modeling, specifically FSI, can be a valuable tool throughout the entire design lifecycle of artificial heart valves, from initial conceptualization to rigorous testing before human implantation. The ability of FSI to accurately model the complex interplay between blood flow and the mechanical behavior of valve components allows for a more comprehensive understanding of device performance under physiological conditions. The numerical FSI analysis was in greater agreement with experimental results than the CFD analysis. Hence, FSI analysis provides more realistic fluid dynamic results than CFD, describing the actual behavior of polymeric heart valves. Malvè et al. [6] investigated outcome differences between FSI and CFD analyses when modeling a healthy human left arterial bifurcation. Using FSI, they examined the effect of wall compliance on coronary hemodynamic regarding wall shear stress. They observed remarkable discrepancies in both the magnitude and profile of wall shear stress between the two modeling approaches for compliant and rigid walls.

Relating with the biomedical applications (human eye and blood flow in arteries) an analogy with the deformation of solid structures under fluid flow in enclosure or channel is significantly affected by fluid–structure interaction, FSI [8]. When fluid flow causes structural deformation, or conversely, when changes in the structure cause flow dynamics to change, FSI occurs. Heat exchange rates, temperature distribution, and pressure drops within the system can be significantly influenced by this dynamic interaction [9]. Because of the fluid's movement, structures respond to the forces applied by the fluid, which modulates their geometry in FSI scenarios. As a primary goal, FSI is often used in heat transfer applications to optimize heat transfer rates and minimize energy losses in devices such as heat exchangers, pumps, or turbines [10]. As a result of internal or external forces exerted by the fluid, deformations in FSI problems can alter the geometry of the enclosure or channel, affecting both the flow field and heat transfer process [11, 12]. FSI is pivotal in several industries, including aerospace, automotive, energy, and biomedical, with applications such as wind turbine blade deformation, airplane wing vibration, blood flow in veins, and cooling electronic devices [13–15].

Convection involving fluid–structure interactions across various boundary conditions and geometries has been extensively studied in the field of heat transfer [16–19]. As an alternative to traditional Lagrangian and Eulerian methods, arbitrary Lagrangian–Eulerian (ALE) techniques have been particularly prominent. As a result of this technique, the computational mesh nodes can move or remain stationary based on the simulation requirements [20, 21]. This adaptability makes the ALE method ideal for simulating complex FSI scenarios, such as the study by [22], who explored natural convection in a vibrating vertical channel and discovered specific frequency and amplitude combinations could reduce convection efficiency [23].

There are many engineering applications that require enclosed cavities, particularly those containing internal obstacles, such as the thermal management of solar panels, cooling of electronics components, thermal insulation, and fuel cells [24–26]. The effects of FSI on heat transfer rates and fluid dynamics within these systems are often studied [27]. While these studies are complex and computationally demanding, they provide insights into the behavior of fluid and structural interactions under natural convection conditions [28, 29]. For instance, Ref. [30] analyzed transient mixed convection in an open cavity with elastic walls, showing that flexible boundaries could enhance heat transfer by up to 17% under certain conditions. As well, Ref. [31] studied forced convection and FSI inside an open horizontal channel with two alternating adiabatic baffles. On the bottom wall of the channel, a constant heat flux was induced, while on the top wall, a thin compliant segment was present. The Nusselt number in a baffled channel was enhanced by nearly 94% by compliant wall segments, highlighting the significant potential for flexible structures in enhancing convection.

It has recently been shown that flexible wall and fin materials are beneficial in thermal systems [32]. Adaptable elements respond dynamically to changes in thermal and mechanical loads, improving the system's ability to modulate heat transfer in real time [33]. Component shapes and elasticity can be customized by engineers so that heat transfer rates are finely tuned to meet specific operational requirements. Studies of natural convection in flexible-sided cavities have shown that the wall's elastic modulus significantly affects heat transfer dynamics [34]. The internal Rayleigh and Hartmann numbers of a flexible-sided triangular cavity showed that an increase in them tends to decrease heat transfer, as shown in a specific study. Additionally, an inclined magnetic field was shown to further suppress convection at high external Rayleigh numbers [35]. The shape of the cavity can also play a role in the management of the energy transfer. The horizontal rectangular channel is regarded as one of the most straightforward and versatile forms of heat exchangers. In this design, thermal energy is exchanged through convective processes between the fluid moving within the channel and its bounding walls [36]. Using a lid-driven trapezoidal cavity in 3D, researchers demonstrated that flexible side surfaces could regulate heat transfer rate, with their elasticity directly proportional to the thermal performance of the cavity [37]. The adaptability of heat transfer introduces a refined method for controlling and optimizing it under various operational conditions [38].

Flexible fins play a notable role in enhancing convective heat transfer. Ref. [39] investigated mixed convection within a trapezoidal chamber using flexible fins and non-Newtonian fluids. Their results showed that shear-thickening fluids, when combined with flexible fins, achieved higher Nusselt numbers at low Richardson numbers. Other studies have examined step-channel configurations with flexible walls positioned at different locations, finding that vertical flexible walls can increase heat transfer by 7.3% compared to rigid walls [40]. These results point to the strategic placement of deformable components as a means of improving system efficiency. Despite the potential benefits of channels and enclosures, challenges still exist in achieving high thermal efficiency [41].

The shape of the cavity can also play a role in the management of the energy transfer. The use of phase change materials (PCMs) in FSI studies adds another layer of complexity and utility. Ref. [42] explored the interaction of PCMs with flexible baffles in a semicylindrical enclosure. Their findings revealed that strong flow circulation, especially at high Reynolds numbers, caused significant deformation of the baffles, resulting in increased heat transfer without excessive pressure drop. Energy storage systems can achieve high thermal performance by combining PCMs with flexible structures [43].

Aside from the typical enclosure designs, recent years have seen significant interest in channels and enclosures with corrugated or wavy walls. The investigation into natural convection within such uniquely structured enclosures has been driven by their extensive application across a variety of industrial and technological fields [44, 45]. Wavy surfaces increase heat transfer area, which enhances thermal energy storage efficiency [46]. Ref. [47] examined the effect of hybrid nanofluids combined with wavy walls on heat transfer in a key study. The researchers detailed how heat is transferred in these wavy enclosures by natural convection and conduction, highlighting the synergy between the walls' physical structure and the hybrid nanofluids' thermal properties. Similarly, Ref. [48] studied the dynamics of free convection in a square enclosure with wavy walls, studying rarefied gaseous flow dynamics. Moreover, their findings highlight the significant impact enclosure shape has on heat transfer mechanisms, asserting that the geometrical characteristics of the walls have a substantial influence on thermal performance.

Focusing the present study on the FSI application in medical field, it is found that most examinations have concentrated on relatively simple benchmarks, excluding the complex interaction between intraocular fluid flow and delicate ocular designs such as the Descemet membrane, particularly in detachment issues.

The current work aspires to fill this gap by designing a comprehensive FSI model that simulates the dynamic interaction between the intraocular fluid and the detached Descemet membrane. Hence, the present analysis presents a further technique by integrating advanced heat-FSI procedures with complicated CFD modeling to investigate the human eye's biomechanical and fluid dynamic behavior under pathological conditions like Descemet membrane detachment. This outcome examines how fluid flow within the eye's anterior chamber interacts with the detached membrane, influencing both its mechanical stability and the overall intraocular pressure. The model shows a more profound experience of the biomechanical consequences of membrane detachment, delivering valuable insights into potential therapeutic strategies and surgical interventions.

Materials and Methods

A model's schematic diagram, along with its coordinate system, is illustrated in Fig. 1. The FSI approach is adopted for the current problem as it brilliant in biological structure, Luraghi et al. [5], where it simulates the interaction between the liquefied vitreous and the DDM. This approach robustly simulates the DDM velocity transmission to the liquefied vitreous, as taken into account by Ferroni et al. [4]. Although saccadic and eye motions affect the fluid dynamics inside the ocular Ferroni, 2020, drug, these two motions are omitted, and the focus is on the fluid motion driven by buoyancy force. For Newtonian incompressible liquefied vitreous, the conservation model can be casted as follow.

$$\nabla^* \cdot \mathbf{u}^* = 0, \tag{1}$$

$$\frac{\partial \mathbf{u}^*}{\partial t} + (\mathbf{u}^* - \mathbf{w}^*) \cdot \nabla^* \mathbf{u}^* = -\frac{1}{\rho_\mathrm{f}} \nabla^* P^* + \nu_\mathrm{f} \nabla^{*2} \mathbf{u}^* + \mathbf{F}, \tag{2}$$

$$\frac{\partial T}{\partial t} + (\mathbf{u}^* - \mathbf{w}^*) \cdot \nabla^* T = \alpha_\mathrm{f} \nabla^{*2} T, \tag{3}$$

where T and P^* correspond to the temperature and pressure fields, respectively, while $\mathbf{w}^* = (u_\mathrm{s}^*, v_\mathrm{s}^*)$ defines the velocity vector of the moving mesh. The fluid velocity vector is represented by $\mathbf{u}^*$. The system's properties include kinematic viscosity ν_f, the density ρ_f, and thermal diffusivity α_f (applicable to both the liquid and the structure). Furthermore, the

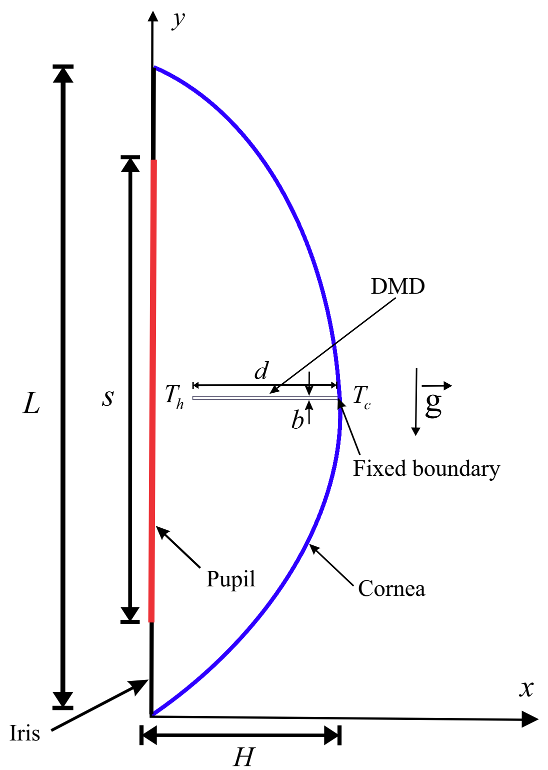

Fig. 1 Physical model of the anterior chamber of human eye and the boundary conditions

body force F accounts to the buoyancy force acting in vertical direction, $\mathbf{F} = (0, \beta \mathbf{g}(T - T_c))$, where $\mathbf{g}$ denotes the gravitational acceleration and β the thermal volumetric expansion coefficient. The bending of the flexible DMD is modeled utilizing [23]

$$\rho_s \frac{d^2 \mathbf{d}_s^*}{dt^2} - \nabla^* \sigma^* = \mathbf{F}_v^*, \tag{4}$$

where σ^*, $\mathbf{d}_s^*$, and $\mathbf{F}_v^*$ correspond to the stress distribution, the displacement of the structural wall, and the applied body forces, respectively. The deformation of the wall structure was modeled using a hyper-elastic framework, with the stress tensor σ^* calculated through the Neo-Hookean constitutive model:

$$\sigma^* = J^{-1} \sum FSF^{\mathrm{Tr}}, \tag{5}$$

in which

$$F = (I + \nabla^* \mathbf{d}_s^*), \quad J = \det(F) \quad \text{and} \quad \sum = \frac{\partial W_s}{\partial \varepsilon}. \tag{6}$$

Here, (Tr) represents the transpose operator. The strain (ε) and its associated energy density (W_s) are defined as

$$W_s = \frac{1}{2}\mu_l (J - I_1 - 3) - \mu_l \ln(J) + \frac{1}{2}\lambda (\ln(J))^2, \tag{7}$$

$$\varepsilon = \frac{1}{2}\left(\nabla^* \mathbf{d}_s^* + \nabla^* \mathbf{d}_s^{*\mathrm{T}} + \nabla^* \mathbf{d}_s^{*\mathrm{T}} \nabla^* \mathbf{d}_s^*\right), \tag{8}$$

where the Lame constants are expressed as $\mu_l = E_\tau/(2(1+\nu))$ and $\lambda = E_v/[(1+\nu)(1-2\nu)]$. In this context, I_1 refers to the first invariant of the Cauchy–Green deformation tensor. The material properties, Poisson's ratio and Young's modulus, are denoted by ν and (E), respectively. At the interface between the wall and the liquid, the boundary conditions were enforced to ensure continuity of displacements and forces:

$$\frac{\partial \mathbf{d}_s^*}{\partial t} = \mathbf{u}^*, \quad \sigma^* \cdot \mathbf{n} = -P^* + \mu_f \nabla^* \mathbf{u}^*. \tag{9}$$

At the interface between the DMD and the liquid, the conditions of thermal equilibrium were applied, ensuring continuity of heat flux and temperature:

$$\frac{\partial T}{\partial \mathbf{n}} \quad \text{and} \quad T = T_c, \tag{10}$$

where $\mathbf{n}$ represents the unit normal vector to the wall.

Next, the following dimensionless variables were introduced:

$$Y = \frac{y}{L}, \quad X = \frac{x}{L}, \quad \theta = \frac{T - T_c}{T_h - T_c}, \quad \mathbf{d}_s = \frac{\mathbf{d}_s^*}{L}, \quad \sigma = \frac{\sigma^*}{E^*},$$
$$\mathbf{w} = \frac{\mathbf{w}^* L}{\alpha_f}, \quad \mathbf{u} = \frac{\mathbf{u}^* L}{\alpha_f}, \quad \nabla = \frac{\nabla^*}{L}, \quad \nabla^2 = \frac{\nabla^{*2}}{L^2},$$
$$t_p = \frac{t_p^*}{L^2}, \quad \tau = \frac{t\alpha_f}{L^2}, \quad P = \frac{L^2}{\rho_f \alpha_f^2} P^*, \quad \mathbf{F}_v^* = \frac{(\rho_f - \rho_s) L g}{E_v},$$
$$E = \frac{E_v L^2}{\rho_f \alpha_f^2}, \quad \rho_r = \frac{\rho_f}{\rho_s}, \quad \mathrm{Ra} = \frac{\mathbf{g}\beta_f \rho_f (T_h - T_c) L^3}{\mu_f \alpha_f}. \tag{11}$$

Although the Rayleigh number is well known in thermal engineering, it has significant utility in biomedical context. This includes the elucidation of natural convection mechanisms within biological systems, contributing to a deeper understanding of physiological heat transfer processes.

The governing equations were converted into their dimensionless representation as follows:

$$\frac{1}{\rho_r} \frac{d^2 \mathbf{d}_s}{d\tau^2} - E \nabla \sigma = E \mathbf{F}_v, \tag{12}$$

$$\nabla \cdot \mathbf{u} = 0, \tag{13}$$

$$\frac{\partial \mathbf{u}}{\partial \tau} + (\mathbf{u} - \mathbf{w}) \cdot \nabla \mathbf{u} = -\nabla P + \Pr \nabla^2 \mathbf{u} + \Pr \mathrm{Ra}\, \theta, \tag{14}$$

$$\frac{\partial \theta}{\partial \tau} + (\mathbf{u} - \mathbf{w}) \cdot \nabla \theta = \nabla^2 \theta. \tag{15}$$

In the above, $\rho_r = \rho_f/\rho_s$ and $\alpha_r = \alpha_f/\alpha_s$ represent the density and thermal diffusivity ratios, respectively, while $\mathrm{Pr} = \nu_f/\alpha_f$ defines the Prandtl number. Furthermore, the effect of buoyancy-driven body forces on the structure was disregarded, leading to $\mathbf{F}_v = 0$.

The scaled boundary constraints for Eqs. (12)–(15) are expressed as

On the hot lens:

$$u = v = 0, \quad \theta = 1, \tag{16}$$

On the cornea:

$$u = v = 0, \quad \theta = 0, \tag{17}$$

On the adiabatic iris:

$$u = v = 0, \quad \frac{\partial \theta}{\partial Y} = 0. \tag{18}$$

For the deformable DMD, the interaction conditions are

$$\frac{\partial \mathbf{d}_s}{\partial \tau} = \mathbf{u} \quad \text{and} \quad E\sigma \cdot n = -P + \mathrm{Pr}\,\nabla \mathbf{u}. \tag{19}$$

The Nusselt number (Nu), a critical measure of thermal exchange, reflects the heat transfer rate into the anterior chamber. The local Nusselt number, describing the thermal exchange at the hot lens, can be formulated through the surface energy balance as follows:

$$\mathrm{Nu} = \frac{hL}{k} = -\frac{\partial \theta}{\partial n}, \tag{20}$$

$$\frac{\partial \theta}{\partial n} = \sqrt{\left(\frac{\partial \theta}{\partial X}\right)^2 + \left(\frac{\partial \theta}{\partial Y}\right)^2}. \tag{21}$$

By integrating the local Nusselt number across the surface, the average Nusselt number ($\overline{\mathrm{Nu}}$) is obtained, which signifies the overall heat transfer rate into the cavity:

$$\overline{\mathrm{Nu}} = \frac{1}{S}\int_0^S \mathrm{Nu}\,\mathrm{d}S. \tag{22}$$

The non-dimensional control equations in Eqs. (12)–(15), along with the initial and boundary conditions in Eqs. (16)–(19), are solved numerically using the Galerkin-weighted residual finite element approach (FEM). The computational domain is divided into triangular elements, which are adaptively refined at different stages, as illustrated in Fig. 2. In the finite element method, the determination of unknown quantities within individual elements relies on their values at the nodes of those elements. Specifically, for approximating solutions for velocity, temperature, and pressure distributions, each of these physical quantities is interpolated using a chosen set of basis functions, denoted as $\left[\boldsymbol{\Phi}_i^k\right]_i^M$,

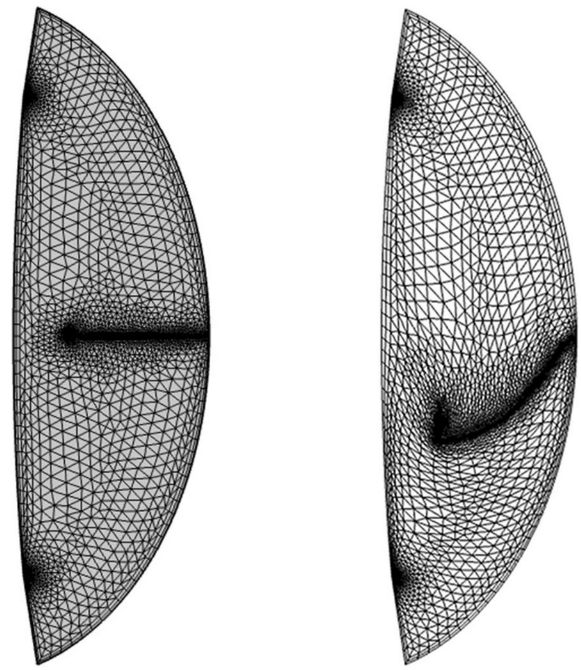

Fig. 2 Distribution of grid points for a mesh size of 5901 at distinct dimensionless time instances: (left) $\tau = 0.001$ and (right) $\tau = 10$

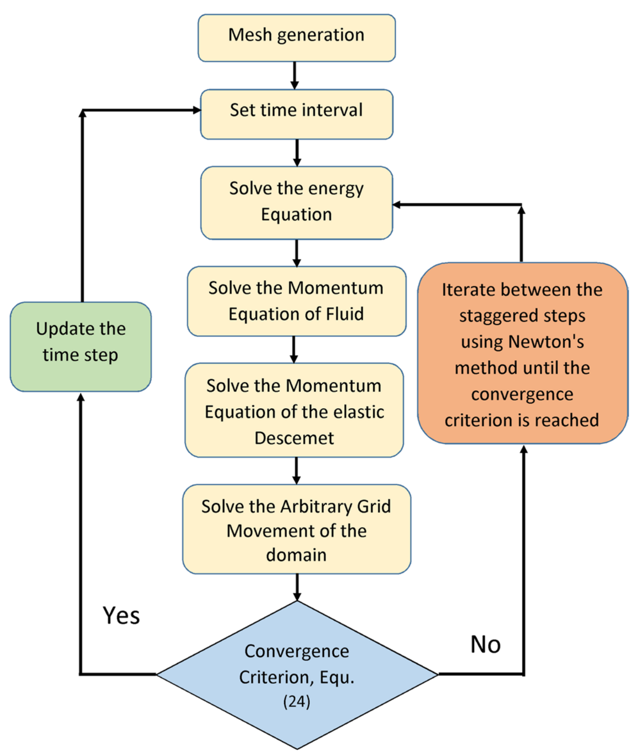

Fig. 3 The summarized procedure of the numerical FEM

$$U, V \approx \Sigma_i^M (U, V)_i^k \Phi_i^k(X, Y),$$
$$\theta \approx \Sigma_i^M \theta_i^k \Phi_i^k(X, Y), \quad (23)$$
$$P \approx \Sigma_i^M P_i^k \Phi_i^k(X, Y).$$

In this context, i serves as an index for individual nodes, k marks the current step in a time-based iteration, and M specifies the overall quantity of nodes. The Newton–Raphson method is employed iteratively to solve the system of nonlinear residual equations that arise from applying the Galerkin-weighted residual approach within the finite element method. This iterative process is crucial for achieving equilibrium in nonlinear (FEA) problems, where the relationship between forces and displacements is not linear. The summarized procedure of the FEM applied in coupling with ALE is depicted in Fig. 3. A detailed description of the finite element method implementation can be found in [49].

Furthermore, for each variable in the system, the iterative solution process continues until the relative error satisfies the following criterion:

$$\left| \frac{\Gamma^{i+1} - \Gamma^i}{\Gamma^{i+1}} \right| \leq 10^{-6}. \quad (24)$$

To validate the current numerical results, a comparison is conducted between the findings of this study and the numerical data from [23] for the fluid–structure interaction (FSI) model and convective heat transfer within a cavity evenly

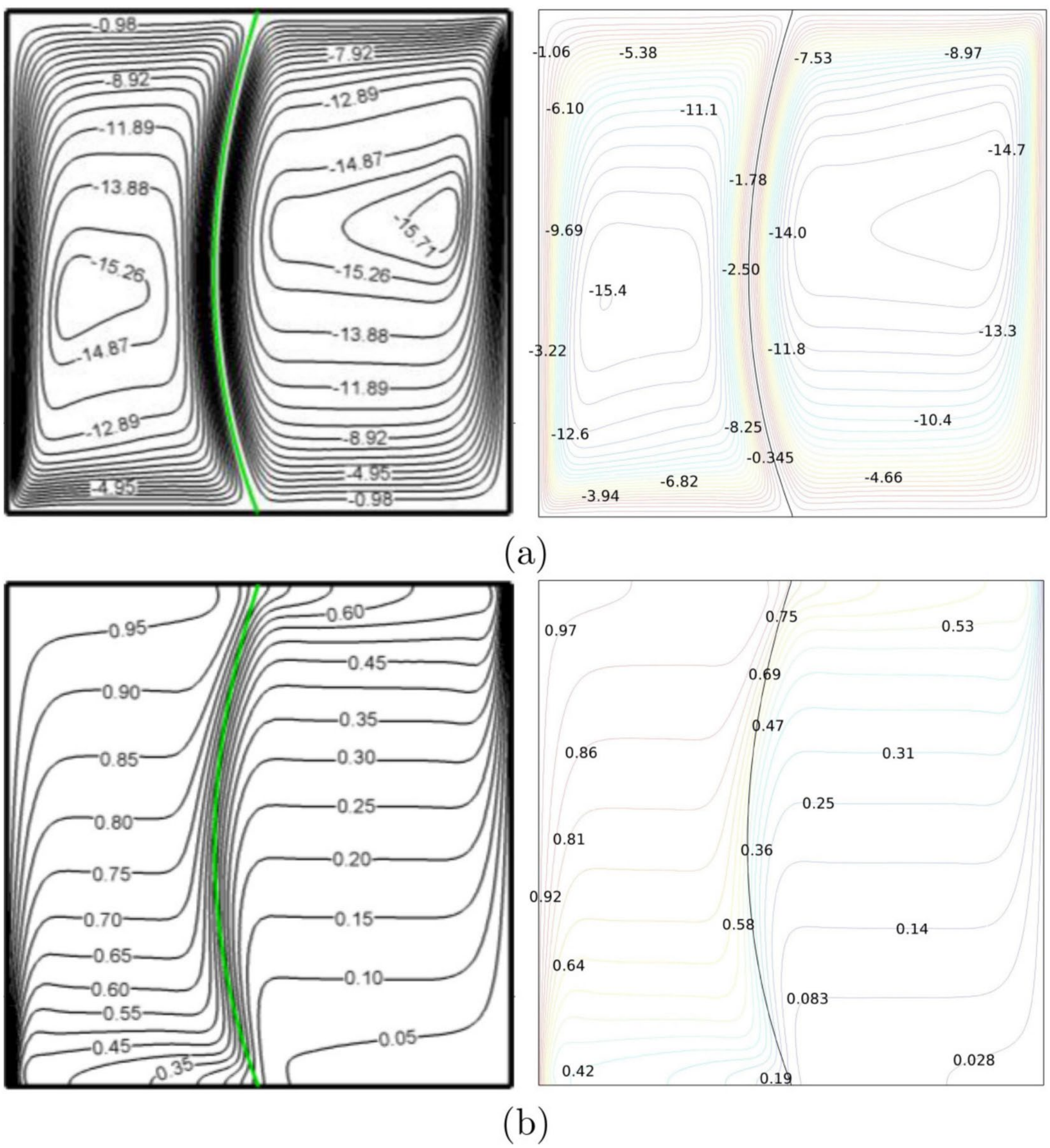

Fig. 4 Streamlines (**a**) and isotherms (**b**); Mehryan et al. [23] (left) and present study (right) for Ra = 10^7, $E = 10^{14}$, and Pr = 6.2

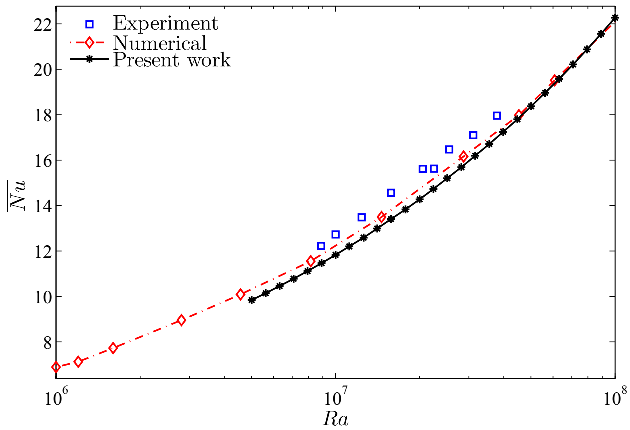

Fig. 5 Comparison among the current overall Nusselt number and the experimental data confirmed by [50] and the numerical outcome according to Churchill's relation by [51] with Rayleigh number toward rectangular cavity at AR = 4 and Pr = 6

partitioned by a flexible membrane. The comparison is performed for $\mathrm{Ra} = 10^7$, $E = 10^{14}$, and $\mathrm{Pr} = 6.2$, as illustrated in Fig. 4. Furthermore, results of the current overall heat transfer have been associated among the experimental outcomes described by [50] and the numerical outcomes that reported by [51] for natural convection flow into a cavity with temperature variation toward side partitions, as exhibited in Fig. 5 when $\mathrm{Pr} = 6.0$. According to these comparatives, it is observed that the aimed outcomes are remarkably into excellent agreement among the results of the earlier published works.

Results

The distribution of the velocity and isotherms within the aqueous humor (AH) are explored with time as shown in Figs. 6 and 7. Figure 6 depicts eight maps of the velocity distribution showing, as assumed, straight DM up to $\tau = 0.01$ with mostly symmetric recirculation surrounding the DDM. Then, when the time progresses the buoyancy force emerges leading to concentrate recirculation at the upper halve of the AC which results in subsiding the DM as the maps of $\tau \geq 0.1$ show. The allocation development of the temperature within the AC with time is shown in Fig. 7. It can be seen from the maps of the figure that at primal times ($\tau = 0.001$ for example), the isotherms are clustered in uniform fashion. As time goes on, the uniformity of the isotherms is disturbed.

Figure 8 demonstrates multicellular (four cells) circulation behavior at $\mathrm{Ra} = 10^3$, while for high Rayleigh number values ($\mathrm{Ra} = 10^5$ and 10^6), the four cells merge in two main cells as can be observed in Fig. 8c, d. On the right hand side of the figure, the isotherms manifest a uniform behavior for $\mathrm{Ra} \leq 10^4$, where the cold isotherms are parallel to the cornea while the hot isotherms parallel to the iris/pupil. For strong convection, $\mathrm{Ra} = 10^5$ (Fig. 8c), the isotherms contract at the pupil region with stratified behavior. For stronger convection, $\mathrm{Ra} = 10^6$ (Fig. 8d), thermal boundary layer looks the thinner in this case.

The effect of the elasticity modulus E of the DDM is investigated in Fig. 9 for $\mathrm{Ra} = 10^5$. The figure presents marginal variations of the velocity distribution and the isotherms as well with varying E despite the alteration of the profile of the DDM.

Figure 10 depicts the variations of the AH circulation and the isotherms with the length of iris (S) at $\mathrm{Ra} = 10^5$ and $E = 10^{10}$. The figure displays that for the lengthy iris (shorter S), the DDM bends down notably as shown in Fig. 10a. Shortening the iris (elongating S), the considered amount of the isothermal heating source produces multicellular behavior of the vitreous liquid, and the thermal boundary layer shrinks due to the DDM, which slightly bends down, as can be observed in Fig. 10d.

The averaged Nusselt number ($\overline{\mathrm{Nu}}$) is adopted to quantify the heat transmission within the AC, moreover, the structural behavior of the DDM and the total displacement of the DDM and the von Mises stress are explored with the dimensionless time τ and other three parameter; Ra, E, and S. Because of the initial condition and progress of heat transfer, Fig. 11a unveils a declined attitude of the $\overline{\mathrm{Nu}}$ with the time. Beyond $\tau = 0.01$, the thermal filed looks stable where the highest Ra number ($\mathrm{Ra} = 10^6$) produces maximum $\overline{\mathrm{Nu}}$ where the percentage rise is 98% when Ra is magnified one order of magnitude than 10^5. As was attributed in Fig. 8, the total displacement of the DDM is greater for higher Ra number as can be seen in Fig. 11b. Raising Ra from 10^4 to 10^5, the displacement is 77% further. Consequently, the stress is also stronger with raising the Ra number as depicted in Fig. 11c.

The time evolution of the $\overline{\mathrm{Nu}}$ for various E's, (Fig. 12a), exhibits marginal influenced heat transfer aspect with E. The total displacement presented in Fig. 12b refers to the tip of the DDM therefore, the ribs seen in the curve at $\tau = 0.01$ exemplifies the fluttering of the DDM. The fluttering case produces a deformed DDM while the tip is almost fixed in position. For this explanation, the von Mises stress magnifies rapidly with raising the elasticity modulus as demonstrated in Fig. 12c, whereas the total displacement does not.

Figure 13a showcases that with shorter iris (longer S, where S accounts for the span of the heat source entering the eye), the convective heat transfer magnifies by 117% when $\mathrm{Ra} = 10^4$ and 78% when $\mathrm{Ra} = 10^5$, both when S expands from 0.2 to 0.6. On the other hand, the bending down of the DDM is significant when $S = 0.2$, where at $\mathrm{Ra} = 10^4$, raising S from 0.2 to 0.4, the DDM percentage deflection is 67.7%, while when S is raised from 0.4 to 0.8, the percentage deflection is 20%. This is due to the difference in the circulations behavior of the vitreous liquid. The von Mises stress manifests almost uniform reduction with increasing S (Fig. 13c).

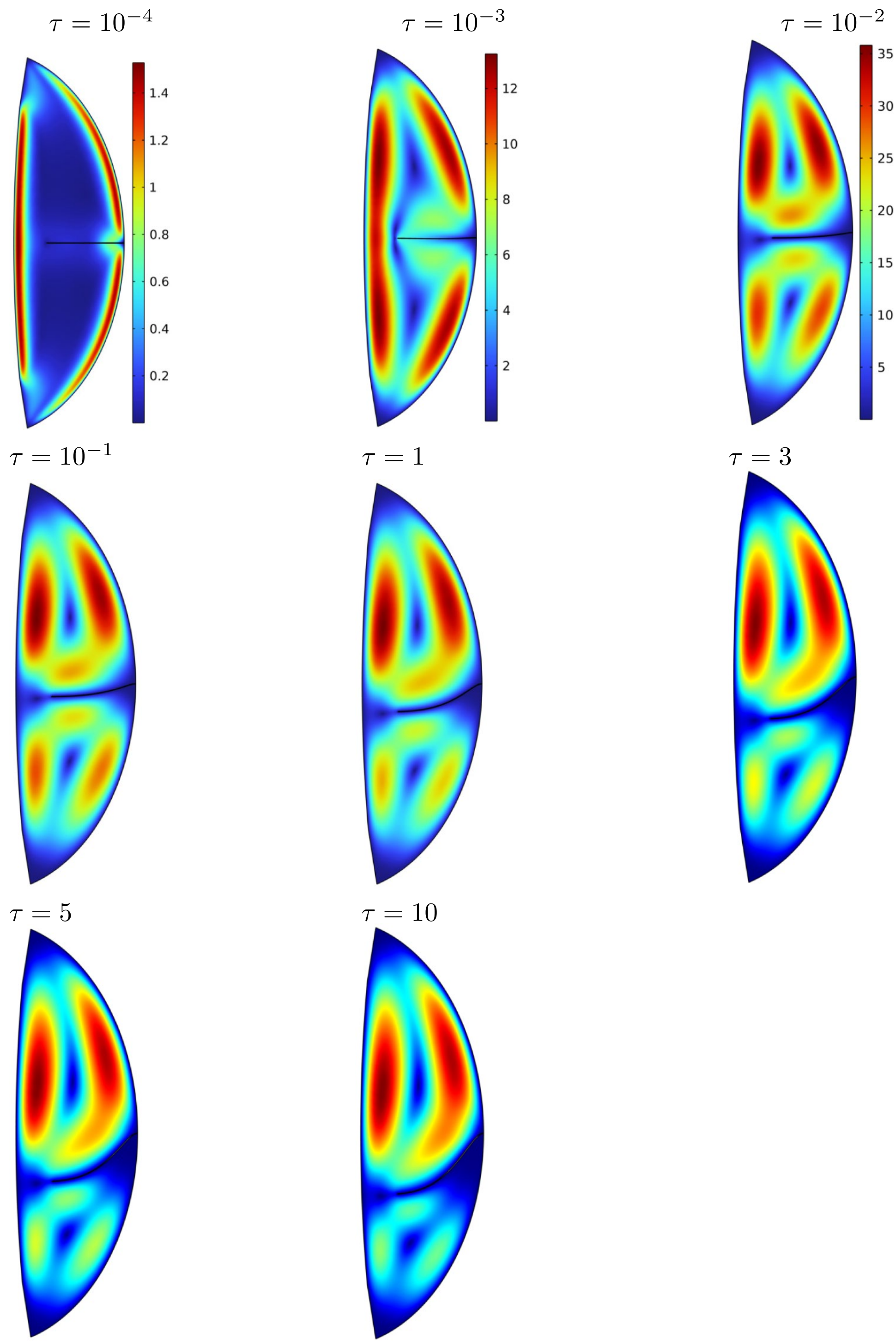

Fig. 6 Time evolution of the velocity at $\mathrm{Ra} = 10^5$, $E = 10^{10}$, and $S = 0.7$

In the same context, the role of the length of the iris is displayed with the modulus of elasticity for $\mathrm{Ra} = 10^5$ as shown in Fig. 14. Figure 14a reveals the uniform rise of the buoyancy augmentation (increasing $\overline{\mathrm{Nu}}$) with shortening the iris (increasing S). The reason that led to this behavior is that the AC is exposed to substantial hot segment represented by the eye lens which is set at the human body constant temperature. Figure 14b emphasizes what was stated in Fig. 13b that is the DDM subsides notably for the lower value of $S = 0.2$, which means the longer iris. Nevertheless, when the elasticity modulus of the cornea is large as $E = 10^{11}$, the drop down of the DDM is mitigated.

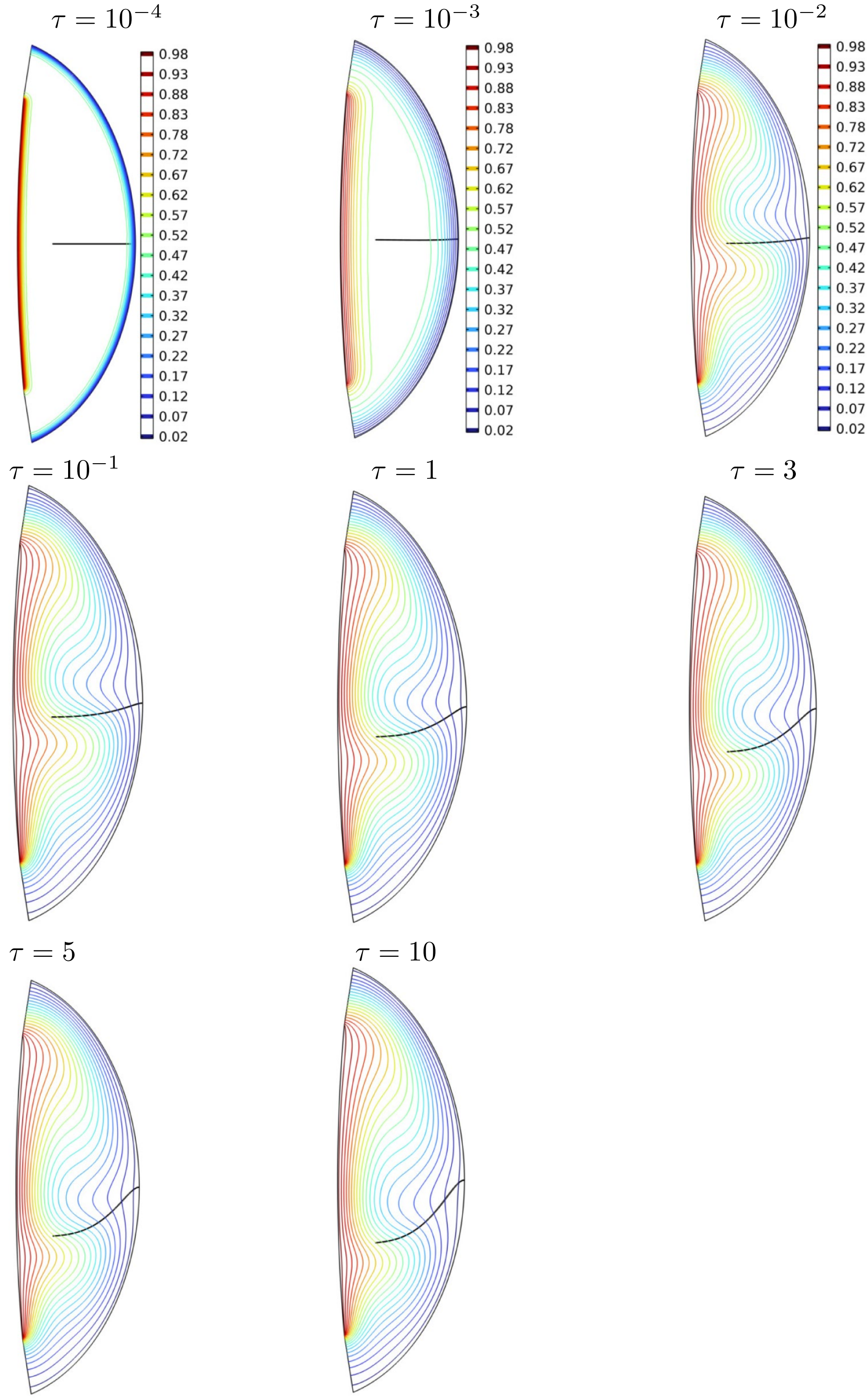

Fig. 7 Time evolution of the isotherms at Ra = 10^5, $E = 10^{10}$, $S = 0.7$

Discussion

The current analysis assumes standing human case, thus the buoyancy inside his eye affects parallel to the wall involving the pupil/iris, which are considered flexible. The detached Descemet membrane (DDM) is assumed to be dangled from the cornea as shown in Fig. 1 and forming a flexible DDM. The aqueous humor (AH) filling the anterior chamber (AC)

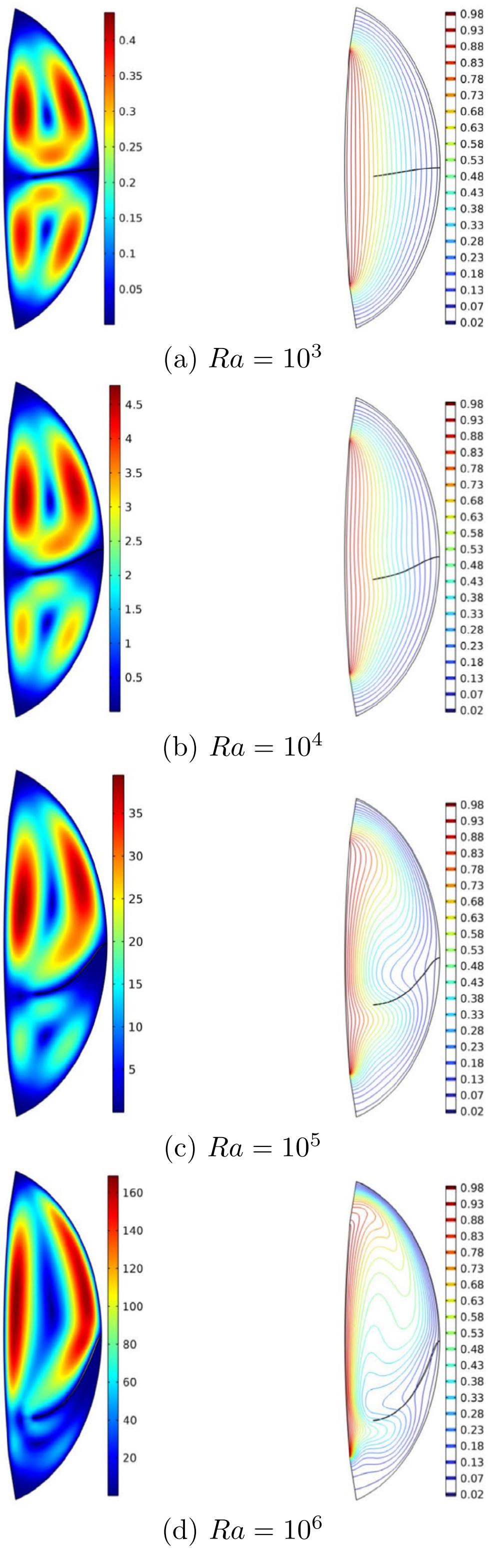

Fig. 8 Variation of the steady velocity (left) and isotherms (right) evolution by Rayleigh number for $E = 10^{10}$ and $S = 0.7$

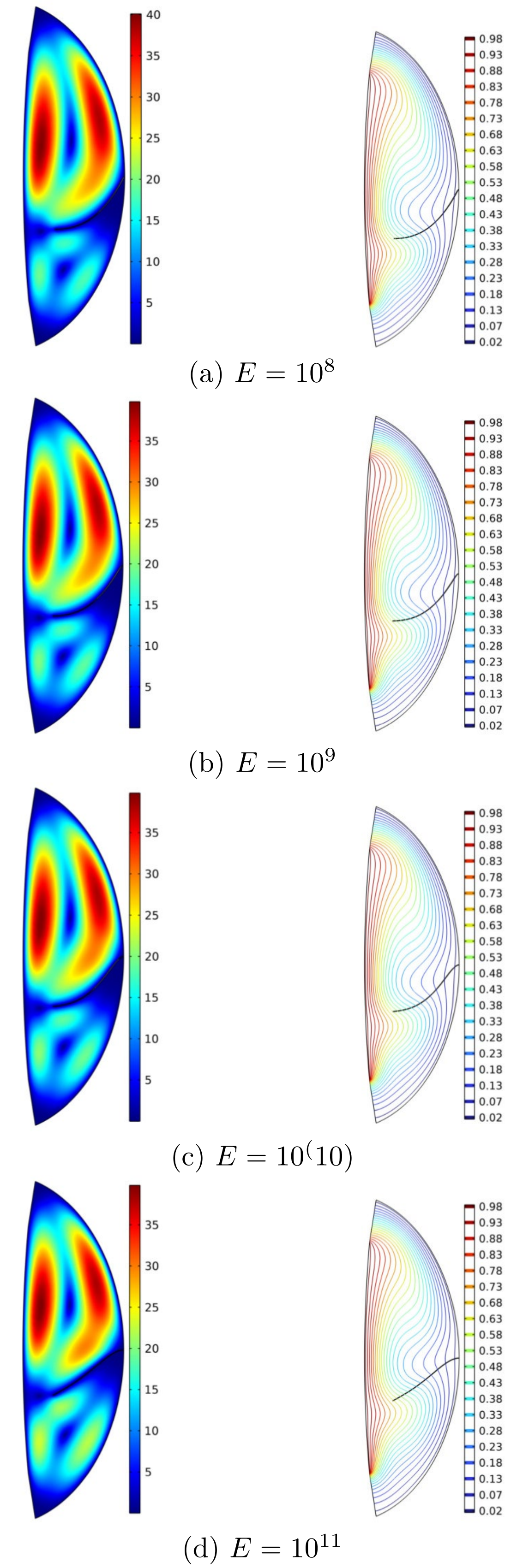

Fig. 9 Variation of the steady velocity (left) and isotherms (right) evolution by elasticity modulus for Ra = 10^5 and $S = 0.7$

Fig. 10 Variation of the steady velocity (left) and isotherms (right) ▶ evolution by the length of iris (S) at Ra $= 10^5$ and $E = 10^{10}$

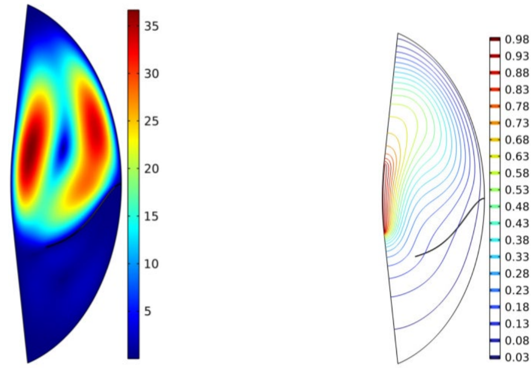

(a) $S = 0.2$

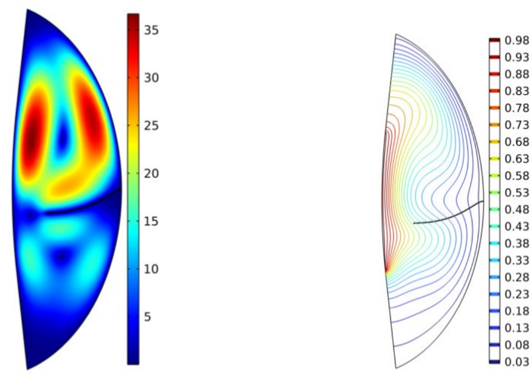

(b) $S = 0.4$

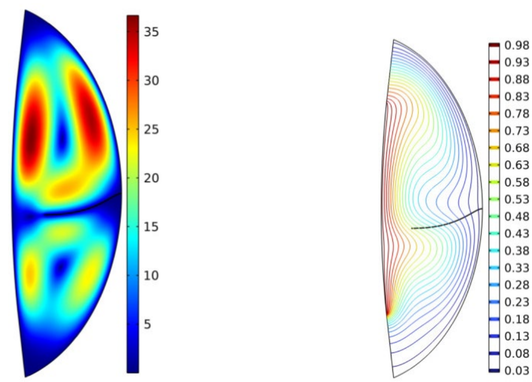

(c) $S = 0.6$

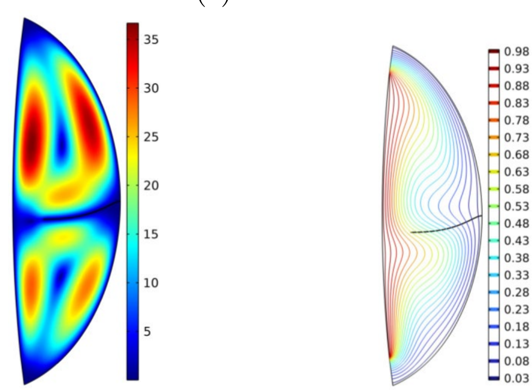

(d) $S = 0.8$

possesses the properties presented in Table 1 [52]. Assuming the dimension $L = 5.5$ mm, the Rayleigh number can be drawn to be Ra $= 4008\Delta T$, therefore varying Ra from 10^3 to 10^6 can be interpreted as varying ΔT within the rage: 0.25, 2.5, 25, and 250 K, forming a thermal treatment. The extensions of the iris is represented by reducing the pupil aperture S. The elasticity modulus is varied from 10^8 to 10^{11} in order to simulate different corneas as a transplantation processes.

From the behavior of the AC, it is demonstrated that the buoyancy force develops with time, leading to concentrated circulation in the upper part of AC and notable bending of the DDM (Fig. 7). This observation aligns with the aneurysm growth over time reported by [32]. In addition, the Rayleigh number plays a pivotal role in emerging the buoyancy force in the AC. As previously mentioned, raising the Rayleigh number is interpreted by raising the temperature difference between the iris/pupil and the cornea. Hence, the significant convection is the main cause of sharp deflection of the DDM. The sharp deflection of the DDM provides free circulation region, which contribute in throwing the thermal boundary layer, which looks the thinner in the higher Rayleigh number. Considering that higher Rayleigh number cases place extra thermal loads on the cornea during operations implementing laser surgery, in practice, care should be taken at high Rayleigh numbers.

Varying the elasticity modulus demonstrates marginal effect upon the thermal and fluid flow (Fig. 9) because of gravity effect along with assumed standing case of human. In this study, the thickness of the DDM is taken to (1.2 mm); however, varying this thickness (left for a future work) may result in different thermal and fluid flow aspects.

People have different iris configurations [53]; therefore, it is wise to explore the length of the iris, which affects, as a result, the length of the contacting part of the lens S having the isothermal hot temperature. For the lengthy iris (shorter S). The isotherms are contracted at the midspan of the AC, leading to dominant recirculation in the upper half of the AC. Consequently, the buoyancy force intensifies above the DDM; thus, it bends. The intensified circulation of the vitreous liquid causes retinal detachment, retinal tears, or bleeding, which is a critical medical case, and may cause vision loss. The isotherms consequently are do not influenced by the DDM.

The excessive increase in the temperature of the vitreous liquid and the deflection of the DDM must be carefully controlled to prevent thermal injury to the eye during clinical procedures and excessive stresses on the DDM. For this reason, the Nusselt number and the total displacement, along with the von Mises stresses, were tracked with the studied

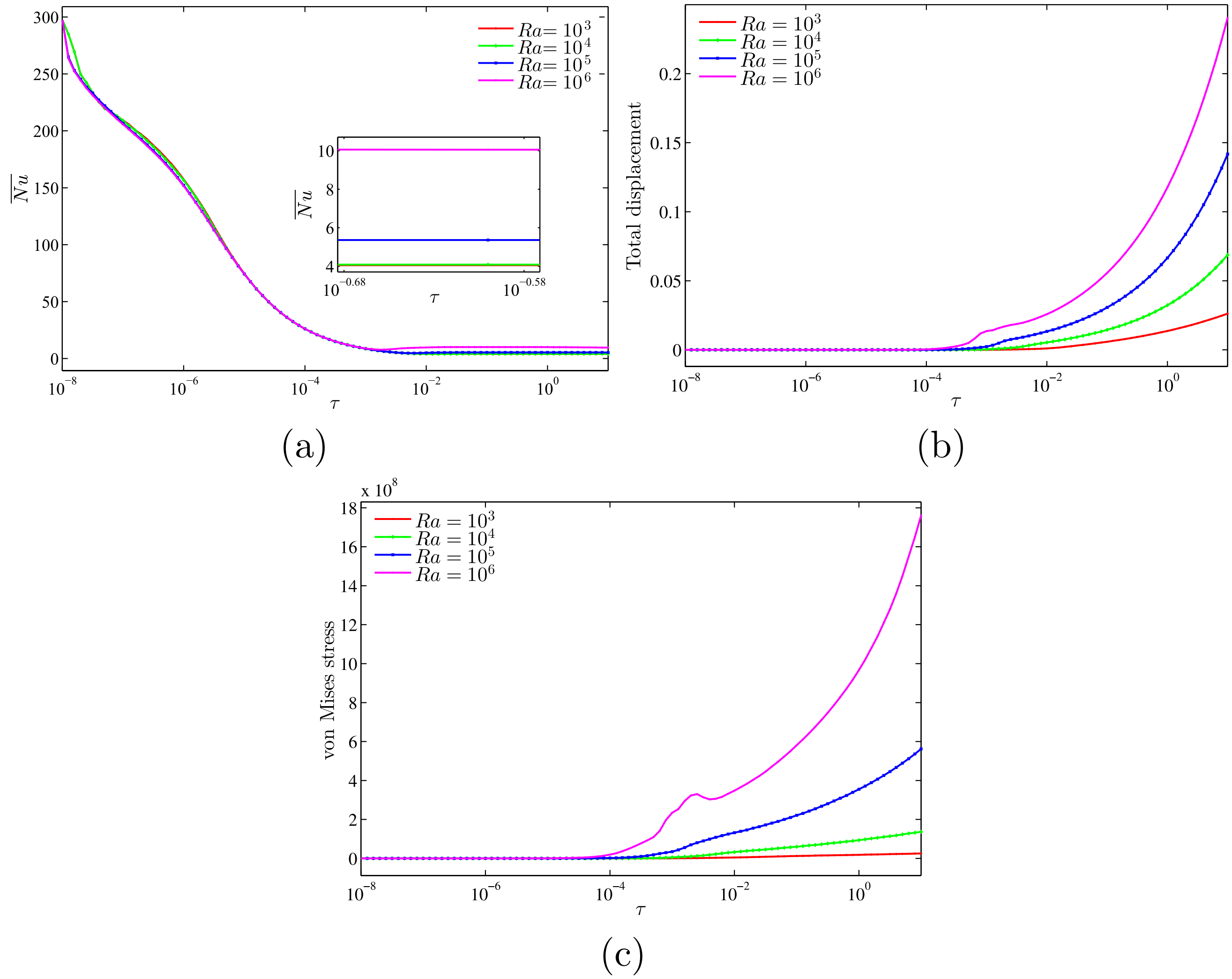

Fig. 11 Variation of the unsteady **a** average Nusselt number ($\overline{\mathrm{Nu}}$), **b** Total Displacement, and **c** von Mises stress with τ for different Ra at $E = 10^{10}$ and $S = 0.7$

parameters (Figs. 11, 12, 13, 14). In this context, the uniform rise of the buoyancy augmentation (increasing $\overline{\mathrm{Nu}}$) with shortening the iris refers to that the AC is exposed to substantial hot segment represented by the eye lens which is set at the human body constant temperature. On the other hand, the ribs of the total displacement that seen at $\tau = 0.01$ exemplifies the fluttering of the DDM. The fluttering case produces a deformed DDM while the tip is almost fixed in position. Moreover, it is sought that the von Mises stress in the DDM is a power function of the elasticity modulus E. This is because the limited deformation in the DDM leads to concentrated stress.

The current study is limited to a 2D analysis and fixed DDM thickness. Future research could expand this study to 3D and investigate variable DDM thickness. Additionally, incorporating the effects of saccadic [3] and eye rotation [4] on the DDM using FSI analysis would provide vital benefit to the medical field of ophthalmology.

Conclusion

This paper explores the FSI analysis of convection within the anterior chamber (AC) of a human eye experiencing Descemet membrane (DM) detachment. The numerical analysis considers coupled heat transmission and fluid flow within a geometry representing the AC, including a flexible membrane representing the detached DM. The study demonstrates that FSI analysis enables the simulation of various elasticity modulus for detached Descemet membrane, an ocular disease, which facilitates the prediction of corneal behavior in transplantation processes. The cornea's elasticity modulus affects the stress imparted on the DDM but not the heat transfer or displacement. The iris's extension lowers the hot segment S, which induces mixed convection

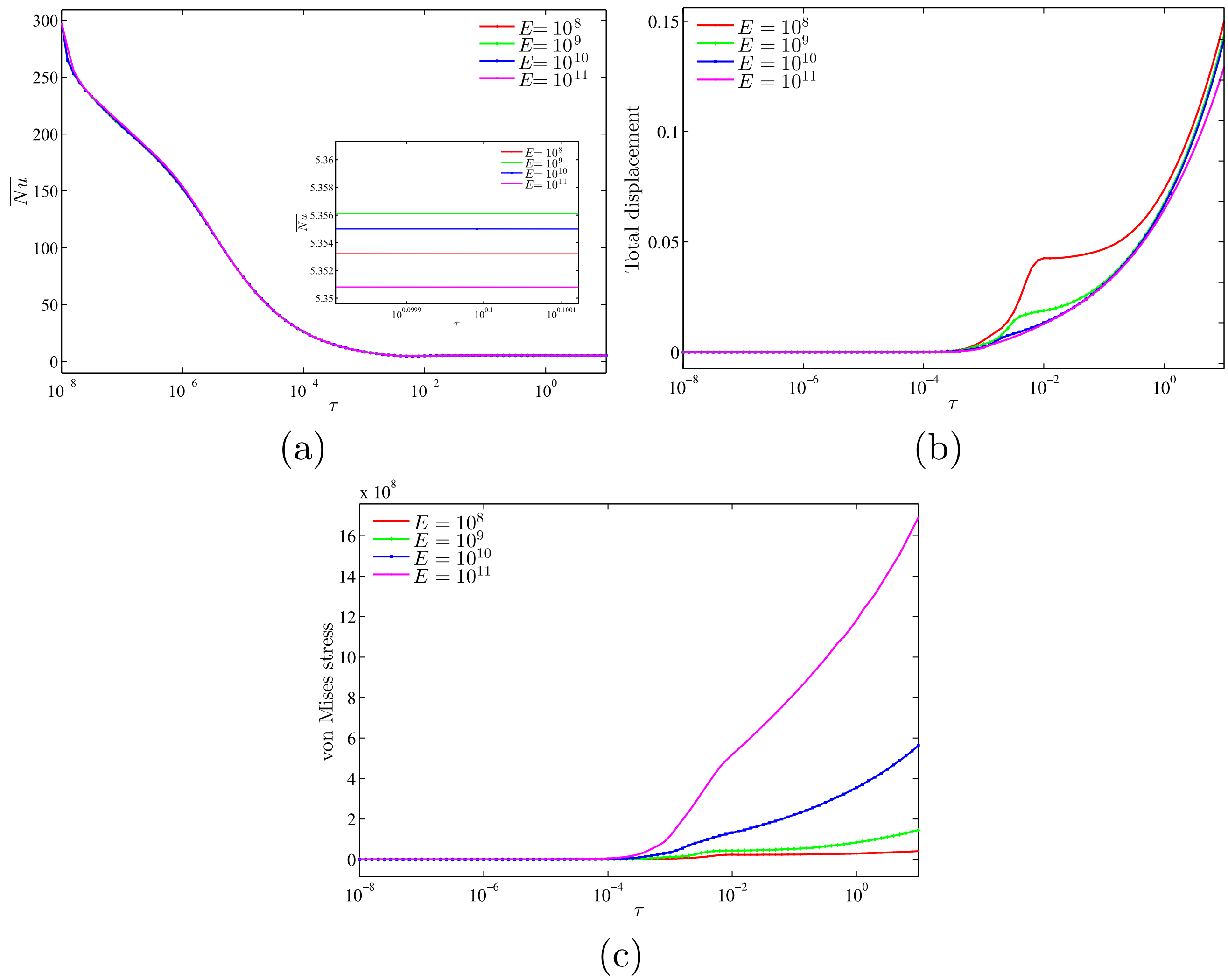

Fig. 12 Variation of the unsteady **a** $\overline{\mathrm{Nu}}$, **b** total displacement and **c** von Mises stress with τ for different E at Ra = 10^5 and $S = 0.7$

within the anterior chamber of the human eye, thereby weakening heat transfer. Consequently, when S increases from 0.2 to 0.6, the average Nusselt number rises by 78% at Ra = 10^5, indicating a significant enhancement in convective heat transfer that must be carefully managed to prevent thermal injury to the eye during clinical procedures. For the general human case, raising the Rayleigh number is proportional to the temperature difference between the pupil and the cornea, according to the relation Ra = $4008\Delta T$. Thus, the thermal treatment of the eye can be interpreted by controlling the Rayleigh number.

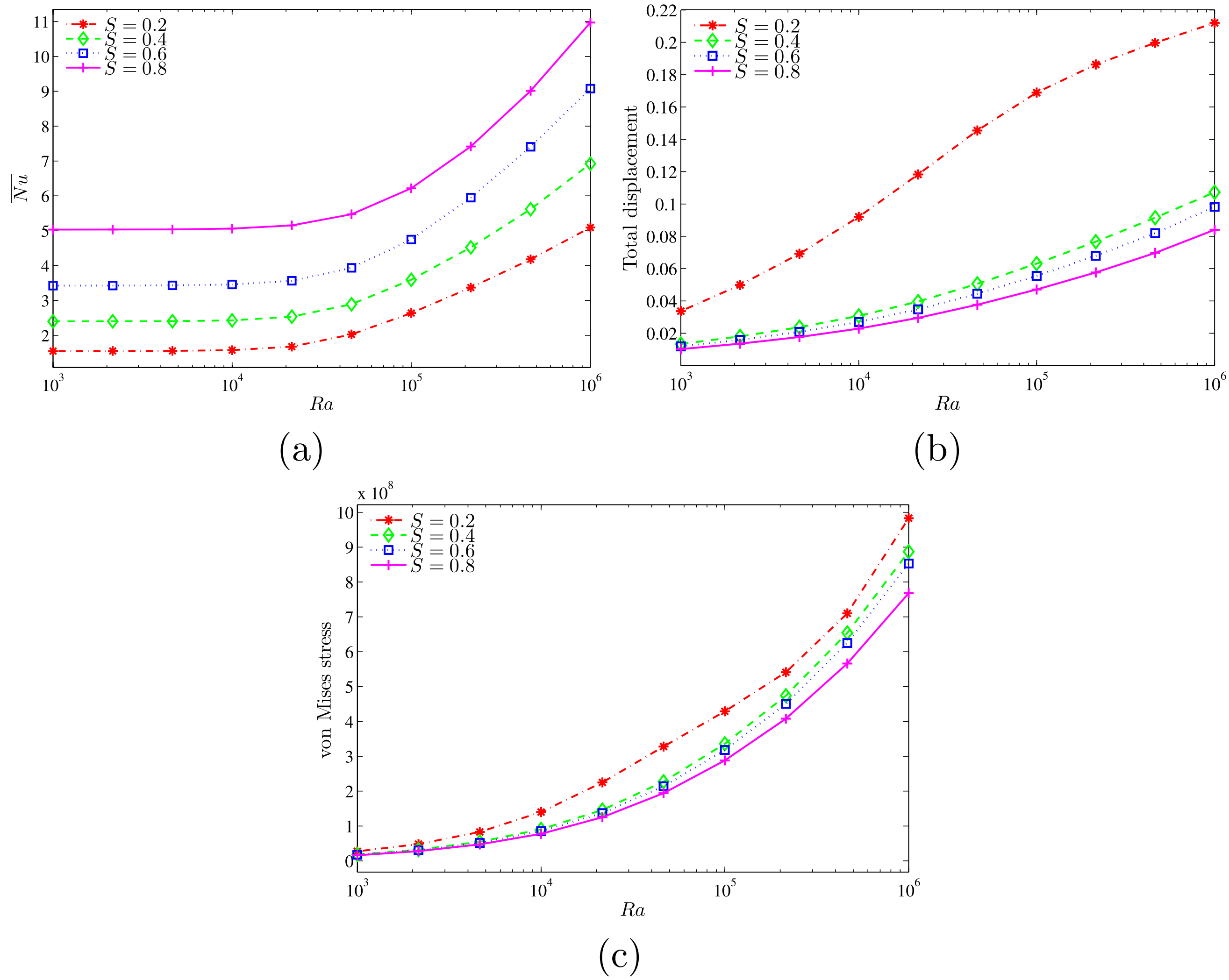

Fig. 13 Variation of the steady **a** $\overline{\mathrm{Nu}}$, **b** total displacement and **c** von Mises stress with Ra for different S at $E = 10^{10}$

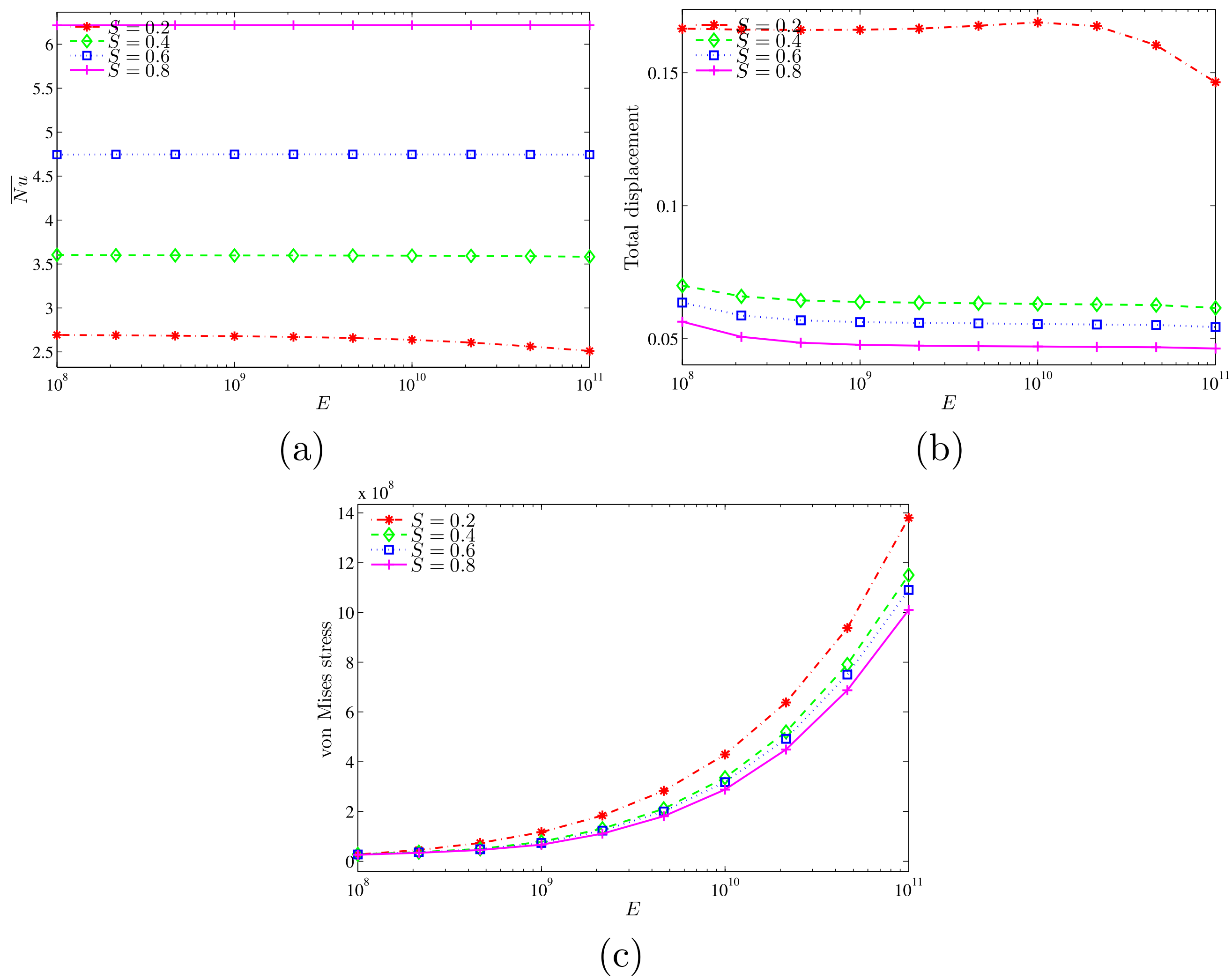

Fig. 14 Variation of the steady **a** $\overline{\mathrm{Nu}}$, **b** total displacement, and **c** von Mises stress with E for different S at Ra = 10^5

Table 1 Physical properties of the aqueous humor, AH [52]

Coefficient of thermal expansion, β (1/K)	3×10^{-4}
Specific heat, C_p (J/kg K)	4200
Viscosity, μ (kg/m s)	0.9×10^{-3}
Thermal conductivity, k (W/m K)	0.57
Density, ρ (kg/m^3)	1000

Author Contributions Ammar Alsabery contributed toward investigation, data curation, and conceptualization. Muneer Ismael contributed to investigation, writing—review and editing, and conceptualization. Zehba Raizah: contributed toward visualization, validation, and methodology. Mohammad Ghalambaz contributed to writing—review and editing, conceptualization, and supervision. Ishak Hashim contributed to review and editing, resources, funding acquisition, and supervision.

Funding The work was supported by the Universiti Kebangsaan Malaysia (UKM) Research Grant GP-2024-K006388. The authors extend their appreciation to the Deanship of Research and Graduate Studies at King Khalid University for funding this work through large Research Group Project under the Grant Number (RGP2/240/47).

Data Availability Not applicable.

Declarations

Conflict of interest The authors declare that they have no conflict of interest.

Ethical Approval Not applicable.

Informed Consent Not applicable.

References

1. Ridha, A. M., M. J. Mohammed, H. A. Saber, M. H. Chyad, and M. H. Abdulameer. Advanced deep learning approaches for early

detection and localization of ocular diseases. *Edelweiss Appl. Sci. Technol.* 8:3708–3721, 2024.

2. Basem, A., D. J. Jasim, Y. A. A. Bahadli, K. Mausam, M. K. Abdulameer, N. K. A. Almasoudie, A. F. Al-Hussainy, A. S. Mansoor, H. Bahair, and A. H. Idan. Impacts of sac centreline length on hemodynamic of anterior cerebral artery for rupture risk analysis via computational study. *Int. J. Mod. Phys. C*. 36:2450215, 2025.
3. Ferroni, M., F. De Gaetano, M. G. Cereda, and F. Boschetti. Evaluation of the ocular fluid dynamic effects on intraocular magnesium-based device: a comparison between CFD and FSI approaches. *Med. Eng. Phys.* 86:20–28, 2020.
4. Ferroni, M., F. De Gaetano, M. G. Cereda, and F. Boschetti. A drug delivery analysis of large molecules in ocular vitreous chamber: dependency on saccadic movements after intravitreal injection. *Med. Eng. Phys.* 82:49–57, 2020.
5. Luraghi, G., W. Wu, F. De Gaetano, J. F. R. Matas, G. D. Moggridge, M. Serrani, J. Stasiak, M. L. Costantino, and F. Migliavacca. Evaluation of an aortic valve prosthesis: fluid–structure interaction or structural simulation? *J. Biomech.* 58:45–51, 2017.
6. Malvè, M., A. García, J. Ohayon, and M. Martínez. Unsteady blood flow and mass transfer of a human left coronary artery bifurcation: FSI vs. CFD. *Int. Commun. Heat Mass Transf.* 39:745–751, 2012.
7. Fadhil, N. A., K. A. Hammoodi, L. Jassim, H. A. Al-Asadi, and L. J. Habeeb. Multiphysics analysis for fluid–structure interaction of blood biological flow inside three-dimensional artery. *Curved Layer. Struct.* 10:20220187, 2023.
8. Hakim, M. A., A. I. Ahad, A. U. Karim, S. Saha, and M. N. Hasan. Fluid structure interaction and heat transfer enhancement with dynamic flexible flow modulator. *Int. Commun. Heat Mass Transf.* 134:105983, 2022.
9. Bathe, K.-J.R. Fluid–structure interactions. *Mech. Eng.* 120:66–68, 1998.
10. Yuan, X., Y. Wang, J. Liu, X. Xu, and X. Yuan. Experimental and numerical study of airflow distribution optimisation in high-density data centre with flexible baffles. *Build. Environ.* 140:128–139, 2018.
11. Ostrach, S. Natural convection in enclosures. In: Advances in Heat Transfer, vol. 8. Amsterdam: Elsevier, 1972, pp. 161–227.
12. Clark, R., D. Cox, H. Curtiss, J. W. Edwards, K. C. Hall, D. A. Peters, R. Scanlan, E. Simiu, F. Sisto, and T. W. Strganac. Modeling of fluid–structure interaction. In: A Modern Course in Aeroelasticity. Cham: Springer, 2005, pp. 491–539.
13. Alsabery, A. I., S. M. Salih, M. A. Ismael, A. K. Hussein, I. Hashim, and J. M. Jalil. Enhancement of cooling process of hot blocks mounted inside a horizontal channel using flexible baffles—alternative arrangement. *Int. J. Thermofluids*. 23:100805, 2024.
14. Hou, G., J. Wang, and A. Layton. Numerical methods for fluid–structure interaction—a review. *Commun. Comput. Phys.* 12:337–377, 2012.
15. Bazilevs, Y., K. Takizawa, and T. E. Tezduyar. Computational Fluid–Structure Interaction: Methods and Applications. Hoboken: Wiley, 2013.
16. Khanafer, K. Fluid–structure interaction analysis of non-Darcian effects on natural convection in a porous enclosure. *Int. J. Heat Mass Transf.* 58:382–394, 2013.
17. Alsabery, A., M. Sheremet, M. Ghalambaz, A. Chamkha, and I. Hashim. Fluid–structure interaction in natural convection heat transfer in an oblique cavity with a flexible oscillating fin and partial heating. *Appl. Therm. Eng.* 145:80–97, 2018.
18. Zargartalebi, H., M. Ghalambaz, A. Chamkha, I. Pop, and A. S. Nezhad. Fluid–structure interaction analysis of buoyancy-driven fluid and heat transfer through an enclosure with a flexible thin partition. *Int. J. Numer. Methods Heat Fluid Flow*. 28:2072–2088, 2018.
19. Alsabery, A. I., H. Saleh, M. Ghalambaz, A. J. Chamkha, and I. Hashim. Fluid–structure interaction analysis of transient convection heat transfer in a cavity containing inner solid cylinder and flexible right wall. *Int. J. Numer. Methods Heat Fluid Flow*. 29:3756–3780, 2019.
20. Rahimi-Gorji, M., T. B. Gorji, and M. Gorji-Bandpy. Details of regional particle deposition and airflow structures in a realistic model of human tracheobronchial airways: two-phase flow simulation. *Comput. Biol. Med.* 74:1–17, 2016.
21. Rahimi-Gorji, M., O. Pourmehran, M. Gorji-Bandpy, and T. Gorji. CFD simulation of airflow behavior and particle transport and deposition in different breathing conditions through the realistic model of human airways. *J. Mol. Liq.* 209:121–133, 2015.
22. Fu, W.-S., and C.-P. Huang. Effects of a vibrational heat surface on natural convection in a vertical channel flow. *Int. J. Heat Mass Transf.* 49:1340–1349, 2006.
23. Mehryan, S. A. M., M. Ghalambaz, M. A. Ismael, and A. J. Chamkha. Analysis of fluid–solid interaction in MHD natural convection in a square cavity equally partitioned by a vertical flexible membrane. *J. Magn. Magn. Mater.* 424:161–173, 2017.
24. Bilgen, E., and H. Oztop. Natural convection heat transfer in partially open inclined square cavities. *Int. J. Heat Mass Transf.* 48:1470–1479, 2005.
25. Wang, J., Y. Zhou, and Q.-H. Deng. Buoyancy-induced flow and heat transfer in multilayered cavities with openings. *Int. J. Numer. Methods Heat Fluid Flow*. 28:1774–1790, 2018.
26. Saha, S., S. Barua, B. Kushwaha, S. Subedi, M. N. Hasan, and S. C. Saha. Conjugate natural convection in a corrugated solid partitioned differentially heated square cavity. *Numer. Heat Transf. A*. 78:541–559, 2020.
27. Ahmed, A. Q., and S. E. Razavi. Enhancing heat transfer in L-shaped enclosures with combined natural convection-fluid structure interaction: incorporating flexible fin and elastic wall. *Numer. Heat Transf. A*. 87(1):2364854, 2024.
28. Soti, A. K., R. Bhardwaj, and J. Sheridan. Flow-induced deformation of a flexible thin structure as manifestation of heat transfer enhancement. *Int. J. Heat Mass Transf.* 84:1070–1081, 2015.
29. Ghalambaz, M., S. Mehryan, R. K. Feeoj, A. Hajjar, I. Hashim, and R. B. Mahani. Free convective heat transfer of a non-Newtonian fluid in a cavity containing a thin flexible heater plate: an Eulerian–Lagrangian approach. *J. Therm. Anal. Calorim.* 147:1809–1824, 2020.
30. Sabbar, W. A., M. A. Ismael, and M. Almudhaffar. Fluid–structure interaction of mixed convection in a cavity-channel assembly of flexible wall. *Int. J. Mech. Sci.* 149:73–83, 2018.
31. Ismael, M. A. Forced convection in partially compliant channel with two alternated baffles. *Int. J. Heat Mass Transf.* 142:118455, 2019.
32. Alsabery, A. I., M. A. Ismael, S. K. Al-Hadraawy, M. Ghalambaz, I. Hashim, and A. J. Chamkha. Fluid–structure interaction model of blood flow in abdominal aortic aneurysms with thermic treatment. *Alex. Eng. J.* 64:81–95, 2023.
33. Pantua, C. A. J., J. K. Calautit, and Y. Wu. A fluid–structure interaction (FSI) and energy generation modelling for roof mounted renewable energy installations in buildings for extreme weather and typhoon resilience. *Renew. Energy*. 160:770–787, 2020.
34. Ismael, M., M. Ghalambaz, Z. Raizah, and M. Fteiti. Fluid structure interaction analysis of counter flow in a partially layered vertical channel of double deformable passages. *Ocean Eng.* 306:118008, 2024.
35. Selimefendigil, F., and H. F. Öztop. Natural convection in a flexible sided triangular cavity with internal heat generation under

the effect of inclined magnetic field. *J. Magn. Magn. Mater.* 417:327–337, 2016.
36. Jaiswal, A. K., and A. Afzal. Design optimization of prismatic rib turbulators in a rectangular channel based on multi-objective criterion. *Int. J. Therm. Sci.* 185:108091, 2023.
37. Selimefendigil, F., and H. F. Öztop. Mixed convection in a partially heated triangular cavity filled with nanofluid having a partially flexible wall and internal heat generation. *J. Taiwan Inst. Chem. Eng.* 70:168–178, 2017.
38. Khanafer, K., and K. Vafai. Effect of a circular cylinder and flexible wall on natural convective heat transfer characteristics in a cavity filled with a porous medium. *Appl. Therm. Eng.* 181:115989, 2020.
39. Yaseen, D. T., and M. A. Ismael. Analysis of power law fluid–structure interaction in an open trapezoidal cavity. *Int. J. Mech. Sci.* 174:105481, 2020.
40. Yaseen, D. T., A. J. Majeed, and M. A. Ismael. Cooling of hot cylinder placed in a flexible backward-facing step channel. *Therm. Sci. Eng. Prog.* 33:101364, 2022.
41. Laouira, H., F. Mebarek-Oudina, A. K. Hussein, L. Kolsi, A. Merah, and O. Younis. Heat transfer inside a horizontal channel with an open trapezoidal enclosure subjected to a heat source of different lengths. *Heat Transf. Asian Res.* 49:406–423, 2020.
42. Salih, S. M., A. I. Alsabery, A. K. Hussein, M. A. Ismael, M. Ghalambaz, and I. Hashim. Melting control of phase change material of semi-cylinders inside a horizontal baffled channel: convective laminar fluid–structure interaction. *J. Energy Storage*. 58:106312, 2023.
43. Alomari, M. A., A. M. Hassan, H. Q. Birdawod, F. H. Ali, H. K. Hamzah, and Q. R. Al-amir. Numerical analysis of NE-phase change material and water mixture in a chamfered cavity with flexible fin. *Int. Commun. Heat Mass Transf.* 161:108520, 2025.
44. Alsabery, A., H. Kadhim, M. Ismael, I. Hashim, and A. Chamkha. Impacts of amplitude and heat source on natural convection of hybrid nanofluids into a wavy enclosure via heatline approach. *Waves Random Complex Media*. 33:1060–1084, 2023.
45. Alsabery, A. I., M. Ghalambaz, A. Hajjar, O. Younis, A. Akremi, M. Fteiti, and I. Hashim. Energy storage and melting heat transfer of coconut oil-CuO aluminum open cell composite embedded in a double wavy wall cavity. *J. Energy Storage*. 98:112875, 2024.
46. Alrasheedi, N. H. Analysis of fluid–structure interaction in the transfer of heat through natural convection within a L-shaped wavy enclosure featuring a movable baffle. *J. Eng. Res.* 13(3):1809–1819, 2024.
47. Revnic, C., T. Groşan, M. Sheremet, and I. Pop. Numerical simulation of MHD natural convection flow in a wavy cavity filled by a hybrid Cu–Al_2O_3–water nanofluid with discrete heating. *Appl. Math. Mech.* 41:1345–1358, 2020.
48. Saleem, K. B., W. Al-Kouz, and A. Chamkha. Numerical analysis of rarefied gaseous flows in a square partially heated two-sided wavy cavity with internal heat generation. *J. Therm. Anal. Calorim.* 146:311–323, 2021.
49. Reddy, J. N. An Introduction to the Finite Element Method, Vol. 2, New York: McGraw-Hill, 1993.
50. Nishimura, T., M. Shiraishi, F. Nagasawa, and Y. Kawamura. Natural convection heat transfer in enclosures with multiple vertical partitions. *Int. J. Heat Mass Transf.* 31:1679–1686, 1988.
51. Churchill, S. W. Free convection in layers and enclosures. In: Heat Exchanger Design Handbook, Section 2.5.8, edited by G. F. Hewitt. New York: Begell House, 2002.
52. Canning, C., M. Greaney, J. Dewynne, and A. Fitt. Fluid flow in the anterior chamber of a human eye. *Math. Med. Biol. J. IMA*. 19:31–60, 2002.
53. Larsson, M., N. L. Pedersen, and H. Stattin. Associations between iris characteristics and personality in adulthood. *Biol. Psychol.* 75:165–175, 2007.